PROCEEDINGS A

rspa.royalsocietypublishing.org

Research

Article submitted to journal

Subject Areas:
mechanical engineering, biomedical engineering, acoustics

Keywords:
shock-induced bubble collapse, high-speed liquid impact, lithotripsy, free-Lagrange method

Author for correspondence:
C. K. Turangan
e-mail: cary@ihpc.a-star.edu.sg

Numerical studies of cavitation erosion on an elastic-plastic material caused by shock-induced bubble collapse

C. K. Turangan[1], G. J. Ball[2], A. R. Jamaluddin[4,†] and T. G. Leighton[3,4]

[1]Fluid Dynamics, Institute of High Performance Computing, Singapore 138632
[2]Atomic Weapons Establishment, Aldermaston, Reading RG7 4PR, UK
[3]Institute of Sound and Vibration research, and
[4]Faculty of Engineering and the Environment, University of Southampton, Highfield, Southampton SO17 1BJ, UK

We present a study of shock-induced collapse of single bubbles near/attached to an elastic-plastic solid using the free-Lagrange method (FLM), which forms the latest part of our shock-induced collapse studies. We simulated the collapse of $40\,\mu$m-radius single bubbles near/attached to a rigid and aluminium walls by a 60 MPa-lithotripter shock for various scenarios based on bubble-wall separations, and the collapse of a $255\,\mu$m-radius bubble attached to an aluminium foil with a 65 MPa-lithotripter shock. The coupling of the multi-phases, compressibility, axisymmetric geometry and elastic-plastic material model within a single solver has enabled us to examine the impingement of high speed liquid jets from the shock-induced collapsing bubbles, which imposes an extreme compression in the aluminium that leads to pitting and plastic deformation. For certain scenarios, instead of the high speed jet, a radially inwards flow along the aluminium surface contracts the bubble to produces a 'mushroom shape'. This work provides methods for quantifying what parameters (e.g. bubble sizes and separations from the solid) might promote or inhibit erosion on solid surfaces.

†Current address: Romax Technology Ltd, Nottingham Science & Technology Park, Nottingham NG7 2PZ, UK

THE ROYAL SOCIETY PUBLISHING

1. Introduction

Shock-induced collapse of gas-filled cavitation bubbles, which results in a formation and impingement of high speed liquid jets, is an extremely violent event. Depending on the shock strength, the jet velocity can reach over 1 km/s [1–5], which is about 10 times higher than the typical velocity of the jets from the inertial collapse of bubbles near solid walls [6]. If the bubbles reside very close or are attached to solid walls, the jet velocity can reach high subsonic or even supersonic speed because of the additional compression of the bubble by the shock reflected by the walls [5]. The jet impact on the solid wall imposes a high stress and strain liquid motion that leads to solid erosion, and eventually a substantial damage if the number of bubbles is high. The pressures generated in the blast wave after jet impact can reach a few GPa [1–5], which further contributes to the overall depression in the solid.

In general, bubble collapse (either shock-induced or inertial) has relevance in surface erosion of fluid machinery [7], underwater explosions [8], kidney stone fragmentation during shockwave lithotripsy (SWL) [4,9] and sensitization of explosives through hot spots [10,11]. For biomedical applications, jetting collapse of cavitation bubbles may offer possibilities of *in vivo* local drug delivery by means of micro-syringe from bubbles loaded with therapeutic agents [12]. It has also been explored for sonolysis of E. Coli and Pichia Pastoris bacteria [13]. However, simply knowing that jetting can be produced is not sufficient because we must also have reliable quantitative methods for predicting where, under what conditions, and how violently it will occur. For example, whilst the ability of such cavitation to destroy cells is valuable in such purposes, if we wish to clean using cavitation without destroying valuable cells (e.g. in ultrasonic cleaning of teeth [14,15] or hands [16]), it is also important to be able to predict what acoustic fields might generate cleaning by bubble activity without damaging other tissues in the vicinity.

Whilst cavitation jets deforming and puncturing a material have been attributed as: the cause of punctures in aluminium foil that has for decades been the favoured proxy used by industry to predict the cleaning potential of a given ultrasonic bath; a possible way to inject drugs into tissue; the cause of pit formation in structures ranging from marine propellers to mercury containment facilities in pulsed neutron sources; there have never been any shock-induced bubble collapse simulations showing this effect. This paper provides this. Furthermore, it provides methods for quantifying what bubble sizes, separations from the solid, and pulse profiles might promote or inhibit erosion, as these cases (ranging from ship or nuclear to biomedical engineering) require.

In experiments, shock-induced bubble collapse has been studied extensively by means of “gas discs" cast in a water-gelatine sheet, which are collapsed with a shock wave from a high speed impactor [2,17]. A similar technique has been adopted elsewhere [18], in which a strong shock wave (e.g. > 100 MPa) was generated to collapse a bubble (2.5 mm radius) to examine the light emission during the collapse. Kodama & Takayama [19] proposed a method in which a small bubble (0.12-3.06 mm radius) placed near a solid gelatin in water was collapsed with the spherical shock wave (10.2 ± 0.5 MPa peak pressure) generated from a laser-induced breakdown. Philipp *et al.* [20] also investigated the interaction of small bubbles (0.15-1.2 mm radius) attached to a $25\,\mu$m-thickness polypropylene foil with a 65 MPa-peak pressure lithotripter shock, which is of our particular interest, and to which a qualitative comparison has been made and presented here. Experimental observation is, however, very challenging even with the use of high speed photography owing to the small spatial and temporal resolution of the collapse events.

Shock-induced bubble collapse involves interconnecting aspects such as compressibility, shock propagation and multi-phases in a highly transient environment, which must be incorporated in the numerical schemes for its simulations. Ball *et al.* [1] simulated the collapse of a 6 mm-dia cylindrical air bubble by a 1.9 GPa-shock using the free-Lagrange method (FLM) to study how the bubble evolves and to examine the thermal characteristics of the collapse events. This work established a methodology for our previous studies in which FLM was further developed to include the axisymmetric geometry for the asymmetric collapse of inertial spherical bubbles near rigid/aluminium walls, shock-induced collapse of $40\,\mu$m-radius bubbles in a free-field and near a

rigid wall, and the coupling of FLM with the Kirchhoff/Ffowcs William-Hawkings formulations to predict the far-field acoustic signatures from the collapse of single/cavitation clouds for the development of a clinical device used during lithotripsy [4,5,21,22]. Other schemes used for shock-induced bubble collapse simulations include the arbitrary Lagrangian-Eulerian [23], level set [24], weighted essentially non-oscillatory scheme [25], front tracking [3], ghost fluid [26] and boundary element methods (BEM) [28] (see [3,4] for the review). For inertial collapse (i.e. underwater explosion type), BEM has been one of the most popular schemes [6,29,30].

The simulations by those schemes with their respective advantages have undoubtedly revealed much of the key characteristics of the collapse events, including the complex shock propagation and interaction inside the bubble and the surrounding liquid, which have been otherwise overlooked in experiments. However, most of those simulations were performed to advance our understanding only in the fluid dynamics aspects associated with the collapse in a free field or near a rigid wall. However, to quantitatively predict the erosion associated with cavitation, the walls must represent real materials whereby the response and the potential damage to the materials can be correctly quantified. As demonstrated in our previous works [4,5], it is the bubbles located very near to a wall that are of particular interest because the presence of the wall has a significant contribution to how violent the collapse can be by inducing a faster jet and higher pressures in the blast wave.

There have been several attempts to simulate the shock-induced collapse of bubbles near physical wall models. Freund *et al.* [31] simulated a collapse of a 20 μm-dia air bubble with a 40 MPa-shock near a “tissue" modeled as a viscous liquid. They showed the progressive motion of the “tissue" in response to jet impingement, but it did not incorporate any structural damage mechanism. Xie & Young [32] also simulated the collapse of a 2D gas bubble by a 2 GPa-shock near a semi-infinite deformable solid. The incident shock and the blast wave propagation in the solid was shown without quantifying the solid deformation. Chahine *et al.* [33,34] and Hsiao *et al.* [35] carried out numerical studies to investigate the solid material erosion caused by the inertial collapse of cavitation bubbles using a hybrid approach: the incompressible BEM code (to capture the bubble dynamics) was coupled with a finite difference code (to quantify the liquid pressures from the collapse events) and a finite element code (to model the solid deformation).

The free-Lagrange method (FLM) used in the present work introduced the ability to simulate the bubble response after the jet impacts the downstream bubble wall, and so predicted the blast wave generated by this [1]. This blast wave contained pressures far in excess of those which occur prior to the jet impact, and so FLM revealed and quantified what is probably the main damage mechanism for solids near such collapses. However, until this paper, FLM could not predict damage from such collapses because it has not incorporated together multi-phases [1,36], the elastic-perfectly plastic response of solids subjected to extreme loading through the incorporation of elastic-plastic material models [36,37] and axisymmetric geometry [4,5,21,38]. This paper incorporates these features within a single solver to illustrate the versatility of the technique for simulating highly transient and deforming multi-phase flows that involve extensive material distortion in solids. This paper aims to allow damage predictions for applications ranging from erosion problems from a century ago [7] to modern ones in neutron generation facilities [39–41], and from opportunities in drug delivery [12] to those in cleaning [16], by simulating the shock-induced collapse of single bubbles attached to rigid and to elastic-plastic solids so as to examine the solid deformation associated with the jetting collapse of the bubbles for various scenarios.

2. Free-Lagrange numerical scheme (FLM) with an elastic-plastic numerical model

The Riemann-based free-Lagrange scheme, *Vucalm*, solves the unsteady and compressible Euler equations derived from the conservation laws for continuous media in a Lagrangian reference frame. The scheme has been well described for 2D planar geometries [1,36,42], including that of the elastic-plastic material model [37]. For axisymmetric geometries, however, the scheme

was only partially described in our earlier works [4,5,21,38]. As the present work focuses more on the mechanisms of solid material deformation associated with bubble jetting, in which the axisymmetric form of the scheme and the elastic-plastic material model are the keys ingredients, the free-Lagrange scheme is (briefly) elaborated as follows. The swirl-free axisymmetric form of the scheme that incorporates the elastic-perfectly plastic flow model is written as

$$\frac{\partial}{\partial t}\int_{A(t)} \overline{U}(r_p\, dA) + \oint_{S(t)} \hat{n}\cdot\overline{F}(r_c\, dS) = \int_{A(t)} \overline{G}\,(r_p\, dA) - \int_{A(t)} \overline{H}\,(r_p\, dA). \tag{2.1}$$

The vectors of conserved variables $\overline{U}$, flux $\overline{F}$ (consists of hydrodynamic flux $\overline{F}_h$ for pressure distribution on the control volume, and deviatoric flux $\overline{F}_s$ for deviatoric stresses acting on the control volume) and source terms $\overline{G}$ and $\overline{H}$ associated with the axisymmetric geometry, are

$$\overline{U} = \begin{bmatrix} 1 \\ \rho\,\bar{u} \\ \rho\,E \end{bmatrix}, \quad \overline{F} = \begin{bmatrix} -\bar{u} \\ \underline{I}\,p - \underline{s} \\ \bar{u}\,p - \bar{u}\cdot\underline{s} \end{bmatrix}, \quad \overline{G} = \begin{bmatrix} 0 \\ \frac{\bar{e}_r\, P_f}{r_p} \\ 0 \end{bmatrix}, \quad \overline{H} = \begin{bmatrix} 0 \\ \frac{\bar{e}_r\, s_{\theta\theta}}{r_p} \\ 0 \end{bmatrix}. \tag{2.2}$$

The variables are described with respect to figure 1 that illustrates the unstructured Voronoi mesh used to discretize the computational domain. Each cell represents a control volume that encloses an individual particle and is bounded by cell boundaries. The time-dependent variables $A(t)$ and $S(t)$ are the area and boundary length of the cell, r_p and r_c are the radial distances of the particle and the cell boundary from the symmetry axis, respectively, $\hat{n}$ is the unit normal vector of the cell boundary, ρ is the fluid density, $\bar{u}$ is the fluid velocity ($\bar{u} = (u, v)$ where u and v are the velocity components in the symmetry axis (x) and radial axis (r), respectively), E is the energy per unit mass ($E = \varepsilon + (\bar{u}\cdot\bar{u})/2$, where ε is the internal energy), $\underline{I}$ is the unit tensor, p is the static pressure, $\bar{e}_r$ is the unit radial vector and P_f is the pressure acting on a control volume for the axisymmetric formulation. The deviatoric stress tensor $\underline{s}$ has 4 components: the normal stresses in the axial and radial directions (s_{xx} and s_{rr}), the shear stress (s_{xr}) and the stress in the circumferential direction or known as the hoop stress ($s_{\theta\theta}$). In the beginning of simulations, each particle is prescribed with thermodynamic conditions, initial conditions and coordinates.

Using the operator time-splitting technique [37], the governing equation (2.1) can be split into the hydrodynamic and deviatoric operators, respectively, i.e.

$$\frac{\partial}{\partial t}\int_{A(t)} \overline{U}(r_p\, dA) + \oint_{S(t)} \hat{n}\cdot\overline{F}_h(r_c\, dS) = \int_{A(t)} \overline{G}\,(r_p\, dA) \tag{2.3}$$

$$\frac{\partial}{\partial t}\int_{A(t)} \widetilde{\overline{U}}(r_p\, dA) + \oint_{S(t)} \hat{n}\cdot\overline{F}_s(r_c\, dS) = -\int_{A(t)} \overline{H}\,(r_p\, dA), \tag{2.4}$$

which are solved sequentially over a single time step to update the flow variables and the stresses. The vectors $\overline{F}_h = [\,-\bar{u} \quad \underline{I}\,p \quad \bar{u}\,p\,]^{\mathrm{T}}$ and $\overline{F}_s = [\,0 \quad -\underline{s} \quad -\bar{u}\cdot\underline{s}\,]^{\mathrm{T}}$ are the hydrodynamic and deviatoric fluxes, respectively, and $\widetilde{\overline{U}}$ is the intermediate value of the conserved variable vector from the solution of equation (2.3). If the medium is not an elastic-plastic solid, the solution of the flow variables from the hydrodynamic operator (2.3) becomes the final values in the new time level. Otherwise, the solution of the flow variables represent the intermediate values of the flow variables, which become the inputs for the deviatoric operator (2.4).

For the axisymmetric geometry of the hydrodynamic operator, the computational cell volume for 1 rad rotation is $V = r_p\, dA = m/\rho$, where m is the mass of the computational cell. For a K-sided polygonal computational cell, equation (2.3) can be written in terms of the present n^{th} and the intermediate time levels to give

$$\widetilde{\overline{U}} = \frac{\widetilde{\rho}}{\rho^n}\left[\overline{U}^n - \frac{\rho^n\,\Delta t}{m}\sum_{k=1}^{K} \hat{n}_k\cdot\overline{F}^n_{h,k}\,(r_{c,k}\,S_k) + \overline{G}\Delta t\right] \tag{2.5}$$

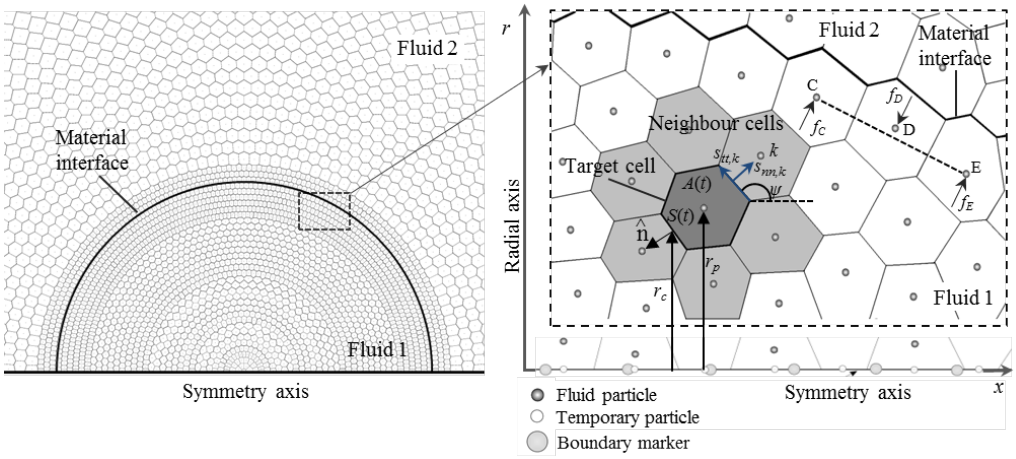

Figure 1. Voronoi mesh used in the simulations. Each cell is a control volume that encloses a single cell-centred particle. It carries an individual fluid type, and is bounded by K cell boundaries that represent K neighbours. Material interfaces always coincide with cell boundaries and no mass transfer is permitted across the interfaces. To update the flow variables (ρ, u, v, T), numerical fluxes across cell boundaries are determined using Riemann solvers of Godunov type. The construction of the edge-oriented normal and tangential stresses for neighbour k (i.e. $s_{nn,k}$, $s_{tt,k}$) is illustrated where ψ is the angle between the cell face and the positive x-axis. An artificial surface tension (an interface smoothing algorithm - see ref. [4,36] for details) is implemented by applying restoring forces f_C, f_D and f_E to particles C, D and E, respectively, so as to move particle D towards an imaginary line joining particles C and E.

where

$$\overline{F}_{h,k} = (A_I)\ \overline{F}^*_{h,k}, \qquad A_I = \begin{bmatrix} \hat{n} & 0 & 0 \\ 0 & \underline{I} & 0 \\ 0 & 0 & \hat{n} \end{bmatrix}, \qquad \overline{F}^*_{h,k} = \begin{bmatrix} -u^*_k \\ p^*_k \\ u^*_k\, p^*_k \end{bmatrix}. \tag{2.6}$$

The cell boundary always coincides with the contact surface of the local Riemann problem in Lagrangian mesh. Therefore, the flow variables (ρ,u,v,T) are updated using equation (2.5) by computing the numerical flux $\overline{F}_{h,k}$ on the k^{th} side of the cell. This is done by solving the 1D Riemann problem on the k^{th} side of the cell boundary to obtain the wave-processed variables (velocity u^*_k and pressure p^*_k) for all cell sides using Riemann solvers of Godunov-type (see [42]). A nominal 2$^{\text{nd}}$ order spatial accuracy is achieved using a piecewise-linear reconstruction of the flow variables with a MUSCL-based slope limiter [43]. Three types Riemann solvers adopted to FLM code [1,37,42] are: the HLLC approximate solver for air-air interfaces, the Riemann solver proposed by Flores & Holt [1,44] for air-water and water-water interfaces, and the non-iterative approximate solver proposed by Dukowicz [45] for solid-solid, solid-air and solid-water interfaces. Dukowicz's Riemann solver can also be used for air-water and water-water interfaces.

The evaluation of the flow variables in the deviatoric step is similar to that of the hydrodynamic step [37]:

$$\overline{U}^{n+1} = \frac{\widetilde{\rho}}{\rho^n}\left[\widetilde{\overline{U}} - \frac{\rho^n\,\Delta t}{m}\sum_{k=1}^{K}\hat{n}_k \cdot \overline{F}^n_{s,k}\left(r_{c,k}\,S_k\right) - \overline{H}\Delta t\right] \tag{2.7}$$

where

$$\overline{F}_{s,k} = \begin{bmatrix} 0 \\ -n_x\, s_{nn,k} + n_r\, s_{tt,k} \\ -n_r\, s_{nn,k} - n_x\, s_{tt,k} \\ -u^*_k\, s_{nn,k} - u_{tt}\, s_{tt,k} \end{bmatrix} \quad \text{and} \quad \overline{H} = \begin{bmatrix} 0 \\ 0 \\ \frac{\bar{e}_r\, s_{\theta\theta}}{r_p} \\ 0 \end{bmatrix}. \tag{2.8}$$

The variables n_x and n_r are the axial and radial components of unit normal vector $\hat{n}_k$ acting on the k^{th} cell boundary, respectively, u_k^* and u_{tt} are the velocities normal and tangential to the k^{th} cell boundary, respectively. As illustrated in figure 1, $s_{nn,k}$ and $s_{tt,k}$ are the edge-oriented normal and tangential stresses, respectively, which are function of angle ψ, and are used to update s_{xx}, s_{rr} and s_{xr} (see [37]). To evaluate $s_{\theta\theta}$, its time derivative is considered [46]

$$\dot{s}_{\theta\theta} = 2\mu\left(\dot{\epsilon}_{\theta\theta} - \frac{1}{3}\frac{\dot{\nu}}{\nu}\right), \tag{2.9}$$

where μ is the shear modulus of the material of interest and $\dot{\epsilon}_{\theta\theta}$ is the time derivative of the strain in the circumferential direction ($\dot{\epsilon}_{\theta\theta} = \dot{r}/r$, where r is the radial distance of the centre of the computational cell from the symmetry axis, $\dot{r} = v$ is the radial velocity), ν is the specific volume and $\dot{\nu}/\nu = \dot{\epsilon}_{xx} + \dot{\epsilon}_{rr} + \dot{\epsilon}_{\theta\theta}$ is obtained from the consideration of continuity, where $\dot{\epsilon}_{xx}$ and $\dot{\epsilon}_{rr}$ are time derivatives of normal strains in the axial x and radial r directions, respectively. Equation (2.9) can be integrated in time to give the hoop stress $s_{\theta\theta}$ at the new time level, i.e.

$$s_{\theta\theta}^{n+1} = s_{\theta\theta}^{n} + \left[2\mu\left(\dot{\epsilon}_{\theta\theta} - \frac{1}{3}(\dot{\epsilon}_{xx} + \dot{\epsilon}_{rr} + \dot{\epsilon}_{\theta\theta})\right)\right]\Delta t. \tag{2.10}$$

Before the updated state of the deviatoric stresses is accepted as the final stress value of the material under consideration, it must be tested against the yield condition, and for which the von Mises yield condition implemented using the method of radial return is adopted. The von Mises yield condition stated in 2D axi-symmetric fixed deviatoric space [46] is given by

$$s_{xx}^2 + s_{rr}^2 + s_{\theta\theta}^2 + 2s_{xr}^2 \leq \frac{2}{3}(Y_0)^2 \tag{2.11}$$

where Y_0 is the yield strength of the material of interest, which must be calculated to determine the elastic-plastic yield of the material. The elastic-perfectly plastic model of a given solid material (assumed to be continuous, homogeneous and isotropic) follows the work-hardening model. The stress is to increase linearly as a function of strain. If the load is released before reaching the material's yield point, the stress returns to its original value and the material is said to be in elastic regime. Beyond that point, the stress will remain constant and equal to the yield point, and the material is considered to flow plastically whereby a permanent deformation occurs [37].

Regarding the equation of state (EOS), air is represented by the ideal gas EOS (i.e. $p = \rho R T$, where p is pressure, ρ is density, $R = 287.14\,\mathrm{J/kg\,K}$ is the gas constant for air and T is temperature), and the water by the Tait EOS (i.e. $p = B\left[(\rho/\rho_\mathrm{R})^\eta - 1\right]$, where $\rho_\mathrm{R} = 999.96\,\mathrm{kg/m^3}$ is the reference density, and $B = 3.31 \times 10^8$ Pa and $\eta = 7$ are constants). The application of these EOS in the present work is based on some assumptions, and their validity and limitations have been discussed by Ball *et al.* [1]. For solids (e.g. aluminium), the Osborne EOS that takes the form of a quadratic fit to experimental data is employed (see [37] for detailed formulation). Here, the heat and mass transfer, viscosity and surface tension have been omitted. The temperature is calculated for the air phase only, which then tends to over-estimate the prediction of temperature inside the bubble. It was argued that the dynamics of the bubble is dominated by the water inertia [1] and the timescale for the main events of the collapse is very short. Therefore, the significant extra computational load taken to include these aspects was not, with current resources, considered commensurate with the extra accuracy they would bring. Additionally, owing to the formulation in axisymmetric geometry, the 3D effects of the flow are not captured.

3. Lithotripter shock-induced bubble collapse simulations

(a) A single bubble attached to a planar rigid wall

Jamaluddin *et al.* [4] simulated the collapse of a single $40\,\mu$m-radius air bubble near a rigid wall by a 60 MPa-lithotripter shock for different stand-off distances. The aim was to assess the role of wall distance in the dynamics of the collapse. The $40\,\mu$m-radius is typical of secondary stable bubbles that have been formed as a result of the interaction of cavitation nucleus with a preceding

lithotripter shock [47]. They found that the presence of the wall seemed to elongate the bubble during collapse. It also increased the jet velocity (and the resulting pressure from the blast wave), which then produced a more violent collapse than when the bubble is in a free field. A question that becomes the impetus of the present work is: What is the collapse like if the bubble is attached to the wall? Apart from the work by Lauer *et al.* [48] who simulated the collapse of a pre-attached bubble on a rigid wall by a pressure difference between the surrounding liquid and the bubble, i.e. an instantaneous collapse of the 'Rayleigh collapse' type, the shock-induced collapse of cavitation bubbles initially attached to solid walls has been surprisingly overlooked.

In our present numerical studies, the 60 MPa-lithotripter shock is used (to be consistent with our previous works [4,21]) whose analytical expression is given by

$$P_s(t) = 2\,P^+\,e^{-\alpha_d\,t}\,\cos\left(\omega t + \frac{\pi}{C_o}\right) \tag{3.1}$$

where $P^+ = 60$ MPa is the peak pressure (at $t = 0$, $P_s = P^+ = 60$ MPa), $\alpha_d = 9.1 \times 10^5\ \mathrm{s}^{-1}$ is the decay constant, $\omega = 2\pi f$ is the radial frequency with $f = 83.3$ kHz, $C_o = 3$ is constant and t is time [49]. This shock is characterized by a 1 μs-compressive and a 5 μs-tensile waves. The shock pressure of 60 MPa is rather high compared to the level that is likely to be generated in tissue [50]. However, it is the level that is typically generated during laboratory experiments (e.g. 65 MPa shock pressure in ref. [20], and 10-100 MPa shock pressure in ref. [12]), which could be used to validate the prediction of this paper (in which bubble dynamics are observed by high speed photography in water and pressure pulses measured by hydrophones placed in it, which is not possible in humans in vivo) and where lithotripter shocks are sent through water baths.

Three cases were simulated based on the dimensionless distance $\xi = d/R_0$ (i.e. 0.75, 0.875, 0.95) where $R_0 = 40\,\mu$m and d is the separation distance between the bubble's centre and the wall. The water and the air bubble were assumed to be initially in equilibrium and standard atmospheric conditions ($p_\mathrm{w} = p_\mathrm{a} = 101.325$ kPa, $\rho_\mathrm{w} = 1000\,\mathrm{kg\,m^{-3}}$, $\rho_\mathrm{a} = 1.2246\,\mathrm{kg\,m^{-3}}$ and $T_\mathrm{w} = T_\mathrm{a} = 288.15$ K). The subscripts 'w' and 'a' refer to water and air bubble, respectively. The surface tension of the fluids was neglected. The evolution of the bubble is shown in figure 2. As many bubble jetting simulations have shown, the bubble's upstream surface accelerates towards the wall to form a jet that pierces the bubble so it forms a toroid (figure 2(e1)). Prior to ref. [5], previous simulations [23,27,28] had had to cease before the moment the jet impacts the bubble's downstream wall, but FLM [4,5,21] showed that this impact produces an intense blast wave containing pressures 2-3 orders of magnitude greater than the original incident shock.

Key features are labelled as follows. Referring to figure 2, initially, the lithotripter shock MS (initiated at a distance of 120 μm from the bubble's centre) impacts the bubble surface and transmits a weak shock TS into the bubble and a strong expansion wave EW into the surrounding water. Overtime, the pressure gradient in the water in the vicinity of the bubble's upstream surface increases. This surface eventually forms a high speed axial jet that moves along the symmetry axis. Inside the bubble, a bow shock SS is created in front of this accelerating jet. Here, the content of the attached bubbles is in direct contact with the solid. Such cases are fundamentally different from the detached bubble scenarios ($\xi > 1$). This is because the impact of the bow shock SS and the jet on the wall is direct as there is no water layer separating the bubble from the wall, which may affect the surface erosion [50]. The jet impact emits a very strong asymmetric blast wave into the surrounding water, which subsequently interacts with the isolated toroidal bubble, causing it to collapse further (e.g. in figure 2(e2,e3)). Prior to jet impact, the bow shock SS forms an oblique reflection inside the bubble (figure 2(d2,d3)). As the wall is not allowed to deform, the jet is redirected in the lateral direction. It consequently forms a radially spreading water splash that propagates out along the wall (figure 2(e2,e3)), similar to the features of a high speed liquid impact on solids [51], e.g. droplet impact on high speed moving objects.

The high speed jet velocity-time histories of these attached bubble cases are plotted in figure 3(a) together with some of detached bubbles (e.g. presented in ref. [4]) and a free field bubble for comparison. The plots indicate that the bubble's upstream surface velocity initially increases in a gradual fashion but then accelerates to form the jet as the bubble contracts. The

curves are almost identical up to $t \approx 0.15\,\mu$s from the initiation but then vary after the reflection of the incident shock by the wall engulfs the bubble. Apart from $\xi = 2.0$ and $\xi = \infty$ (free field) whose jet velocity only reaches $< 1.4\,$km/s, the other cases have jet velocities exceed $2\,$km/s.

The time histories of the pressure loading on the wall (see figure 2(b2)) for different distances ξ plotted in figure 3(b) shows that in general, for detached bubbles ($\xi > 1$), the peak pressure decreases significantly as ξ increases. A pressure of about $6.7\,$GPa is recorded when $\xi = 1.0625$. It then drops to $2.5\,$GPa when $\xi = 1.25$ and to $0.5\,$GPa when $\xi = 2.0$. For attached bubbles with $\xi = \{0.95, 0.875, 0.75\}$, the pressure loading on the wall are of similar order of magnitude (between 5 and $9\,$GPa). Their pressure time-histories are characterised by two major peaks that are separated by a $0.01\,\mu$s duration. The first peak represents the blast wave emitted when the jet impacts the wall, and the second peak is associated with the pressure wave implosion at the symmetry axis. This high pressure wave that strengthens as it moves radially inwards along the wall towards the symmetry axis (labeled "X" in figure 2(e3)) is found to be originated from the complex reflection of the blast wave by the toroidal bubble and the rigid wall. For $\xi = 0.75$, the pressure can reach

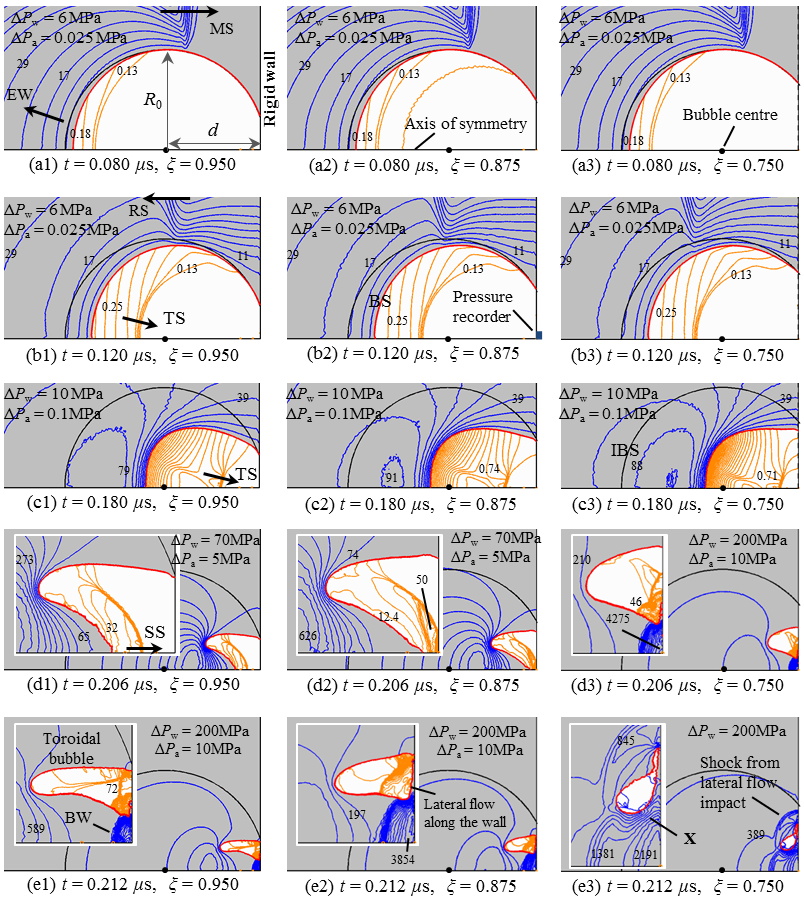

Figure 2. The plots of pressure contours showing the interaction of the bubble with the lithotripter shock for three different distances $\xi = d/R_0$. The bubble elongates because of the additional compression by the shock reflection. Label MS denotes the lithotripter main shock, EW is the expansion waves, RS is the reflected shock and TS is the transmitted shock. Their directions are indicated by arrows. IBS is the initial bubble surface and BS is the current bubble surface. The bow shock SS is formed inside the bubble in front of the accelerating jet. The jet impacts the wall with a velocity $> 2\,$km/s, generating a blast wave BW and a lateral jet sheet (splash) along the wall. Inset is the close-up view of the event.

as high as 9 GPa. Another slightly weaker pressure peak recorded after the second major peak is associated with the rebound of the toroidal bubble.

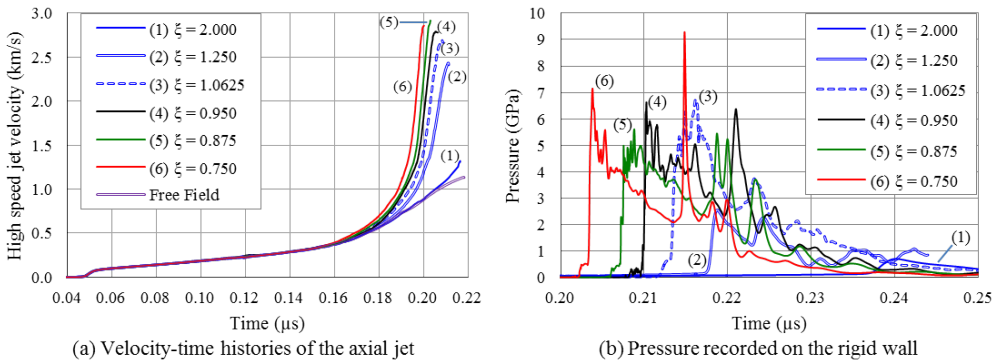

(a) Velocity-time histories of the axial jet (b) Pressure recorded on the rigid wall

Figure 3. (a) The velocity-time histories of the high speed axial jet of the bubble. (b) The pressure loading-time histories recorded on the rigid wall along the symmetry axis (figure 2(b2)) are characterised by two major peaks: the first represents the blast wave emission from the jet impact, and the second is associated with the pressure wave implosion at the symmetry axis. The 60 MPa-lithotripter shock is initiated at a distance of $120\,\mu$m from the bubble's centre (see figure 4).

(b) Single bubbles near and attached to an aluminium wall

When the bubble is attached to an elastic-plastic solid, the collapse dynamics are different from those with a rigid wall because the structural changes to the solid caused by the jet impingement affect the local flow field. Here, aluminium is used as the elastic-plastic solid

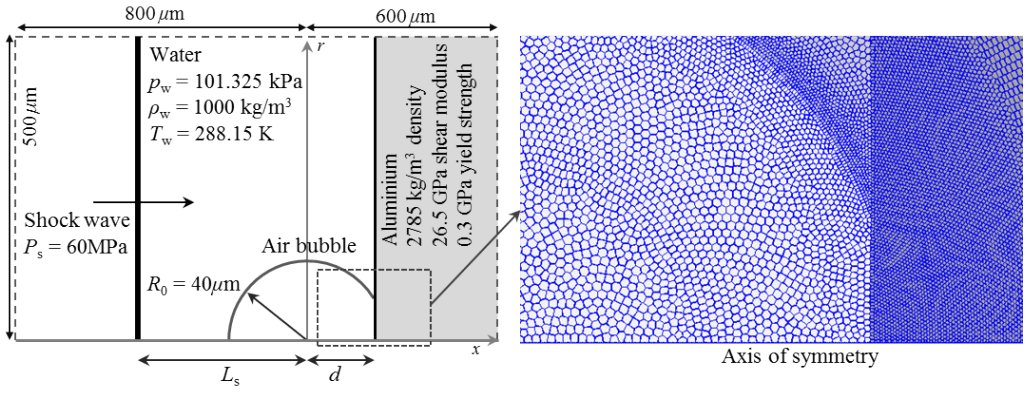

Figure 4. The computational domain of a bubble attached to an aluminium (bubble centre's non-dimensional distance from the aluminium $\xi = d/R_0$), and a close-up view of the Voronoi mesh around the attachment region. L_s is the distance of the lithotripter shock from the bubble's centre at $t = 0$. Apart from the axis of symmetry (solid boundary), non-reflecting inflow/outflow boundary conditions are applicable to the other domain boundaries. The fluids and solid involved are initially at standard atmospheric conditions. The artificial surface tension [36] that helps to suppress the amplitude and growth rate of small scale perturbation of mesh-induced wavenumber instabilities on material interfaces is applied to air-water interfaces only because for solid materials, interface deformation is not influenced by these mesh-induced errors [37].

with properties: $\rho_{\text{al}} = 2785\,\text{kg/m}^3$, shear modulus $\mu_{\text{al}} = 26.5\,\text{GPa}$ and yield strength $Y_0 = 0.3\,\text{GPa}$. As illustrated in figure 4, a 60 MPa-peak pressure lithotripter shock (see eq. (3.1)) propagates towards the bubble. The radius $R_0 = 40\,\mu\text{m}$ of the fully spherical bubble is used as a scaling parameter. At $t = 0$, the shock is generated at a distance $L_s = 120\,\mu\text{m}$ from the bubble's centre. Twelve generic cases were simulated, i.e. $\xi = d/R_0 = \{2.0, 1.5, 1.25, 1.125\}$ for detached bubble and $\xi = \{0.95, 0.875, 0.75, 0.5, 0.25, 0, -0.25, -0.5\}$ for attached bubble. The simulation time starts from when the shock is initiated at $L_s = 120\,\mu\text{m}$. A non-dimensional interface smoothing gain α associated with the restoring force for the artificial surface tension was determined by trial and error from some preliminary simulations with different values tested (i.e. $\alpha = 10, 100, 1000$). It is dependent on how fine the mesh around the air-water interface is. The gain $\alpha = 100$ that corresponds to a maximum correction of about 0.01% to the interface particle displacement for every time step was optimum, whereas $\alpha = 10$ was too low that interface wrinkles were still apparent, and $\alpha = 1000$ was quite excessive that it produced a slightly earlier collapse.

(i) Free field vs rigid wall vs elastic-plastic wall (aluminium)

We first compare the bubble's morphological changes and the surrounding flow field of the case of bubble attached to an elastic-plastic solid ($\xi = 0.95$) with the cases of bubble in a free field and that is attached to a rigid wall. For the aluminium wall case, the domain is initially discritized using $49,293$ computational cells (4920 for air bubble, $33,055$ for water and 11,318 for aluminium), for the bubble in free field case using $45,764$ cells (5056 for air bubble and $40,708$ for water)

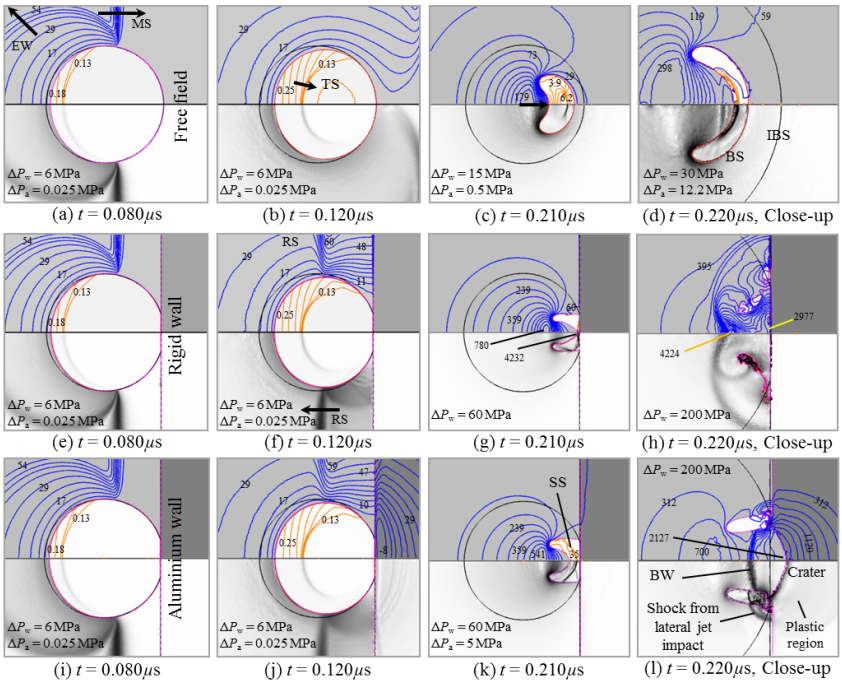

Figure 5. A comparison of the shock-induced collapse of a single bubble in a free field and that attached to a rigid and aluminium walls showing the plots of pressure contours and Schlieren-like at different times. The shock MS is reflected back in the water as a shock RS by the walls, and is also partially transmitted into the aluminium. The bubble's upstream surface forms a high speed jet that accelerates towards the wall, and on impact it generates a blast wave BW. The transmitted shock in the bubble TS, initial bubble surface IBS, current bubble surface BS and bow shock SS in the bubble are labeled accordingly. The directions of the waves and high speed jet are shown. The pressure contour unit is in MPa.

and for the rigid wall case using $37,975$ cells (4920 for air bubble and $33,055$ for water). These computational cells are deemed to be sufficient to capture the physics of the shock-induced bubble collapse, as shown in our previous work in mesh resolution studies [4]. The simulation time-step is controlled by the CFL (Courant-Friedrichs-Lewy) number, and CFL ≤ 0.4 has been used.

At $t = 0.08\,\mu$s (in figure 5), the flow patterns are similar in all three cases. At $t = 0.12\,\mu$s, the lithotripter shock MS has traversed the bubble in a free field, it has been fully reflected by the rigid wall and has been partially reflected by the aluminium. The full reflection of the shock MS by the rigid wall results in a slightly stronger reflected shock RS compared to the weaker reflection when the wall is aluminium. Consequently, the region behind reflected shock RS (between the wall and the bubble's surface) has a slightly higher pressure than that with the aluminium. In the rigid and aluminium wall cases, the reflected shock RS further compresses the collapsing bubble but the effects are more profound for the case with rigid wall, causing the collapse to be faster as indicated by an early high speed jet impact seen at $t = 0.21\,\mu$s (figure 5(g)). The jet impacts the wall directly, emitting an intense blast wave and turning the bubble into a toroid. At $t = 0.22\,\mu$s, while the high speed jet is yet to impact onto the opposite side of the bubble in a free field (figure 5(d)), the jet has already pierced the bubble attached to the rigid wall and induced a lateral motion for the now-toroidal bubble that is seen sliding outwards along the wall (figure 5(h)). However, for the aluminium wall case, the jet impingement produces a crater (and plastic deformation) in which the toroidal bubble is being drawn into by a vortex ring (figure 5(l)).

(ii) The collapse of bubble with $\xi = 0.95$

The evolution of bubble with $\xi = 0.95$ is shown in figures 6 and 7. From the shock initiation until when the bubble is drawn into the creater, the duration lasts about $0.24\,\mu$s. This is less than the compressive wave duration of the lithotripter shock MS of $1\,\mu$s, which means that the events are confined within the compressive wave period. When the shock MS with 60 MPa peak pressure impacts the aluminium, it does not cause any plastic deformation because the pressure is significantly less than the 0.3 GPa yield strength of the aluminium model. Instead, the transmitted shock in the aluminium manifests into an elastic or longitudinal wave that propagates with a velocity $c = \sqrt{E_{\text{al}}/\rho_{\text{al}}}$, (where E_{al} and ρ_{al} are the Young's modulus and density of aluminium). The presence of the bubble that blocks the shock MS imposes a tension (negative pressure) in the aluminium around the contact surface, as shown in figure 5(j).

After impacting the aluminium, the incident shock MS is partially reflected back into the water as a shock wave RS. When the reflected shock RS hits the bubble's surface near the contact line, it is also partially reflected back as an expansion wave (figure 6(c)), and thus lowers the pressure in this region. This appears to keep the contact line of the bubble on the aluminium unchanged. The propagation of reflected shock RS on the bubble's surface imposes a shear that not only squeezes the bubble further but also tends to elongate it. When the bubble contracts, the transmitted shock TS inside the bubble strengthens as a result of a focusing effect induced by the contracting bubble surface. At $t = 0.16\,\mu$s, the bubble is now fully submerged in a high pressure field behind the reflected shock RS. The bubble's upstream surface then accelerates downstream.

At $t = 0.20\,\mu$s, the bubble's upstream surface has flattened, and the bow shock SS starts to form inside the bubble in front of the jet. At $t = 0.21\,\mu$s, the bow shock is arriving at the aluminium surface and is intersecting with the transmitted shock TS that has just been reflected back by the wall. The jet impacts the aluminium with a 2.16 km/s velocity, i.e. 23% lower than the 2.8 km/s velocity when the wall is rigid (figure 3). This supersonic jet impact on the wall emits a blast wave BW that further contracts the now-toroidal bubble at $t = 0.22\,\mu$s. Multiple waves are seen at $t = 0.225\,\mu$s, but they eventually merge into one. The vortex ring surrounding the toroidal bubble draws the bubble into the crater formed by the jet impingement. The crater area is the same as the bubble's contact surface, and the crater depth is $\sim 13.7\,\mu$m (i.e. 34.3% of the bubble radius R_0).

The change in the bubble's shape and surrounding flow field during the final stage of the collapse is shown in figure 7. The computational mesh evolves as it mimics the flow. Inside the bubble, a dense mesh is formed in front of the accelerating jet, which represents a compressed

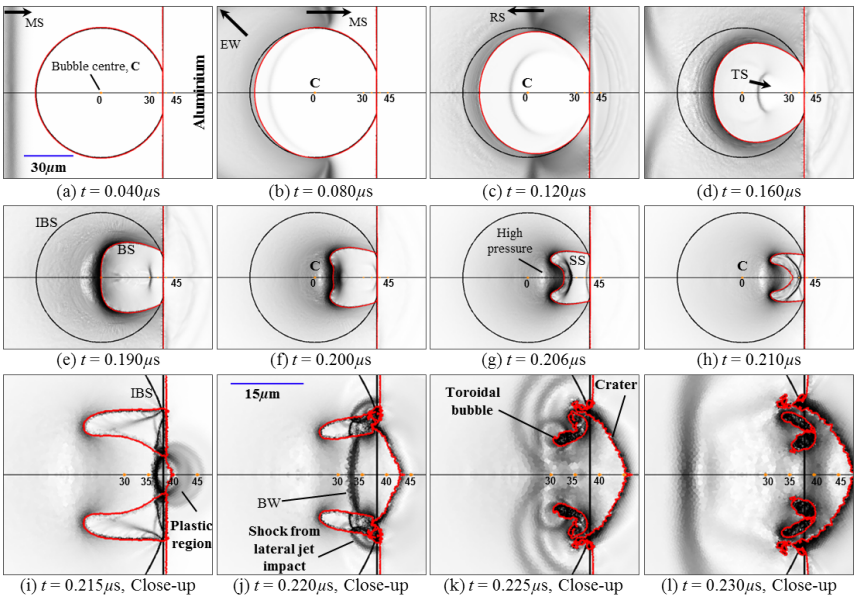

Figure 6. Schlieren-like (density gradient) plots of bubble evolution after its interaction with a 60 MPa-lithotripter shock MS ($R_0 = 40\,\mu$m, $\xi = 0.95$). The incorporation of the compressibility, multi-phases, axi-symmetric geometry and elastic-plastic material model within a single solver has enabled us to examine the impingement of high speed liquid jets that impose an extreme compression in the aluminium, which forms a crater and produces plastic deformation.

region in the bubble. Instead of redirecting the jet along the aluminium surface (as in the rigid wall case), the lateral jet sheet (splash) from the impact is directed in an oblique fashion (at $t = 0.218\,\mu$s) because the aluminium deforms. This jet sheet eventually splits out a small fraction of the bubble adjacent to the aluminium (see the frame sequence of figure 7(f-j)).

For the aluminium (modelled using the elastic-perfectly plastic model), its morphological changes are strictly subjected to satisfying the yield condition given by equation (2.11). Here, the impact of 2.16 km/s jet imposes an extreme compression in the aluminium that, under this circumstance, starts to behave like a fluid whereby a permanent deformation in a form of a crater is produced. From $t = 0.222\,\mu$s onward, when the jet continues to penetrate, the aluminium cells are squeezed out around the tip of the jet. This occurs to such an extent that these cells are stretched to the point whereby tensile forces cannot be transferred to them. At this stage, the aluminium material fails and undergoes a 'numerical fragmentation' and the cells become separated from the main bulk of aluminium as they are ejected out. This exhibits patterns similar to those observed in the high velocity projectile impacts by Howell & Ball [37]. The damage associated with this shock-induced collapse is more profound than the one caused by the inertial collapse (an underwater explosion type) e.g. in the simulation by Chahine *et al*. [34], primarily because of the vast difference in the jet velocity between these two types of collapse.

The use of Voronoi mesh that convects with the local flow velocity results in the dynamic change of the mesh topology that requires frequent re-meshing to prevent mesh distortion. How smooth the material interfaces (defined by the boundaries shared between dissimilar materials) is determined by the mesh resolution around them. The aluminium crater formed after the jet impact (figures 6(i-l) and 7(e-p)) when looked closely, is not very smooth, which is inherent to the use of finite numbers of computational cells. Generally, the characteristics of the fluid phenomena observed agree with the experimental evidence [52,53] and is a high pressure analogy of the response of bubbles to pressure gradients that are observed at lower amplitudes. Such behaviour

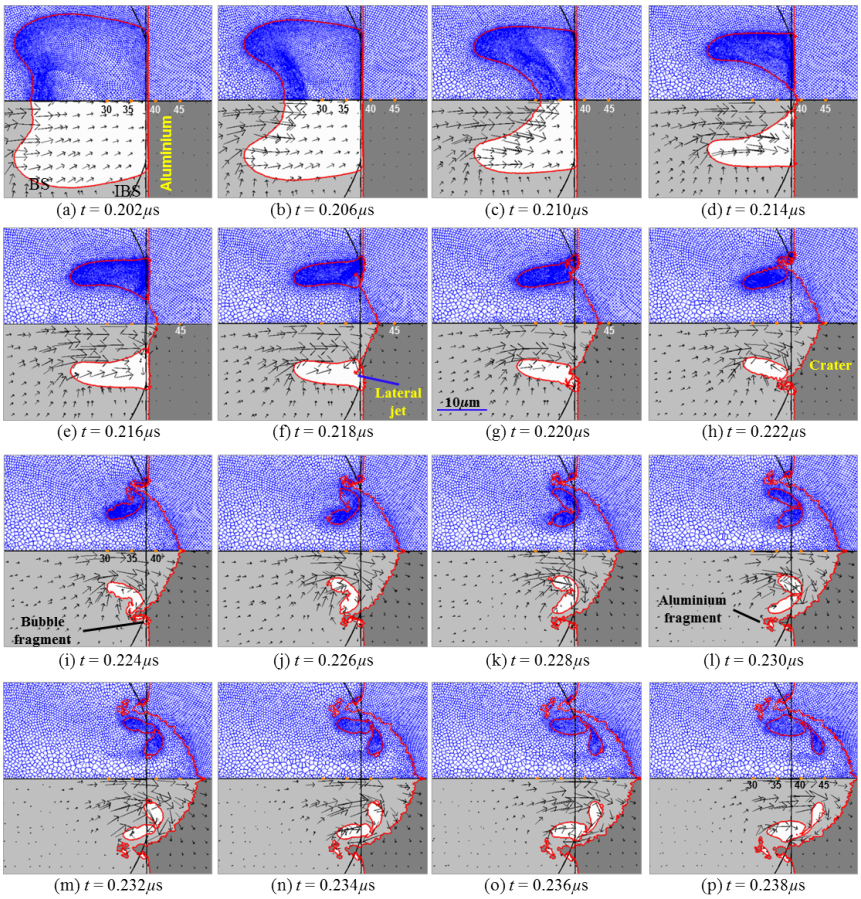

Figure 7. The plots of Voronoi mesh and velocity vectors of the bubble after the high speed jet has fully formed. It shows how the jet impact occurs and the bubble turns into a toroidal shape. The jet impact forms an oblique lateral jet sheet that propagates away from the symmetry axis, which helps to split the bubble section that is attached to the aluminium. The jet impingement creates a crater and squeezes out some aluminium fragments. The bubble is then drawn into the crater by the vortex ring. The vertical solid line represents the original surface of the aluminium at $t = 0$.

has practical implications when multiple shocks are projected at a solid and may cause crack propagation and the fragmentation of solids, which might be desirable (as in lithpotripsy [9]) or undesirable (as in pulsed neutron sources [40]). With sufficient computational resources, for example, this approach would allow investigation of the role in erosion of the survival of bubble nuclei between shocks and the nucleation of cavitation by subsequent (lithotripter [9]) shocks.

(iii) Comparison of the collapse patterns for different distances ξ

The response of the bubble following its interaction with the lithotripter shock MS is examined for 12 case studies, i.e. $\xi = \{2.0, 1.5, 1.25, 1.125, 0.95, 0.875, 0.75, 0.5, 0.25, 0, -0.25, -0.5\}$, that have been designed to represent both the attached ($\xi \leq 1$) and detached bubbles ($\xi > 1$), aimed to evaluate how the distance ξ affects the collapse patterns. Negative values of distance ξ represent the bubbles whose size is less than half of its fully spherical size. Owing to the relative distance of the aluminium surface from the bubble's centre, the interaction varies from case to case.

As depicted in figure 8 at $t = 0.12\,\mu$s, for the detached bubbles i.e. $\xi = \{2.0, 1.5, 1.25, 1.125\}$, the interaction of the weak reflected shock and the right side of the bubble creates a low

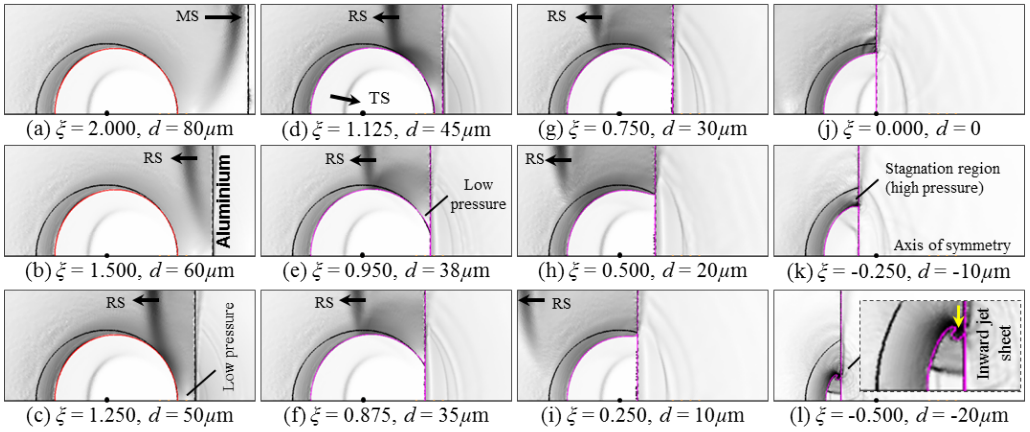

Figure 8. Schlieren-like plots of the interaction of the lithotripter shock MS with the bubble at $t = 0.12\,\mu$s show the features of shock interaction with the bubble and the wall, and the subsequent bubble's evolution for detached bubbles with $\xi = \{2.0, 1.5, 1.25, 1.125\}$ and attached bubbles with $\xi = \{0.95, 0.875, 0.75, 0.5, 0.25, 0, -0.25, -0.5\}$.

pressure region in the water that separates the bubble from the aluminium. This drop in pressure also occurs for the cases of attached bubbles ($\xi = \{0.95, 0.875, 0.75, 0.5\}$), resulting in a nearly unchanged contact line of the bubble on the aluminium. As ξ reduces further ($\xi = \{0.25, 0, -0.25, -0.5\}$), this pressure drop vanishes. The stagnation region behind the reflected shock RS (with pressure nearly double than the pressure of the shock MS) causes the contact line of the bubble to move radially inwards. For $\xi = \{0, -0.25, -0.5\}$, this leads to the 'pinching' of the bubble as its surface near the contact line accelerates to form the inward jet flow (figure 8(l)).

Referring to figure 9, the collapse features and damage patterns can be grouped into: (a) detached bubbles with $\xi > 1$, (b) attached bubble with $0 < \xi \leq 1$, and (c) attached bubble with $\xi \leq 0$. The depth of the craters is plotted in figure 10(b). For $\xi = 2.0$, there is no noticeable depression in the aluminium as the considerably thick water layer (that separates the bubble from the aluminium) helps preventing the jet from impinging and damaging the aluminium even though the blast wave BW from the jet impact is still able to strike the aluminium. For $\xi = 1.5$, there is only a minimal depression in the aluminium, which is caused primarily by the blast wave BW. It is similar for $\xi = 1.25$ but the depression is more obvious. For $\xi = 1.125$, however, the depression is significant as it is produced by both the blast wave and jet impact.

For the attached bubbles with $\xi = \{0.95, 0.875, 0.75, 0.5\}$, the structural damage to the aluminium is fundamentally different from that of detached bubbles. Here, the damage exhibits characteristics similar to those of high speed projectile impacts [37]. The aluminium subjected to the impingement of liquid jets moving at very high velocities ($> 2\,$km/s) behaves like a fluid. The impact produces a crater, and from which some aluminium fragments are squeezed out from the surface. The redirection of the jet upon impact onto the aluminium, which results in the formation of an oblique jet sheet, is also evident. The bubble with $\xi = 0.25$, however, produces a crater similar to the one with $\xi = 1.125$. However, for $\xi = 0.25$, apart from the high speed axial jet, an inward-moving radial flow along the aluminium surface is also formed.

For the attached bubbles with $\xi \leq 0$ (e.g. 0, -0.25, -0.50), the collapse is characterised by the absence of the high speed axial jet and the presence of the inward-moving radial flow along the aluminium. The pinching of the bubbles by this radial flow, whose velocity e.g. for $\xi = -0.25$ can be as high as $1.8\,$km/s, forms mushroom-like shapes (figure 9(j,k,l)). As the pinching strengthens, the bubbles undergo an extreme compression. The pressure in the bubbles can be extremely high as the radial flow approaches the horizontal axis. However, our simulations with $\xi \leq 0$ were not continued beyond the times given in figure 9(j,k,l) because of the precaution imposed on the use of

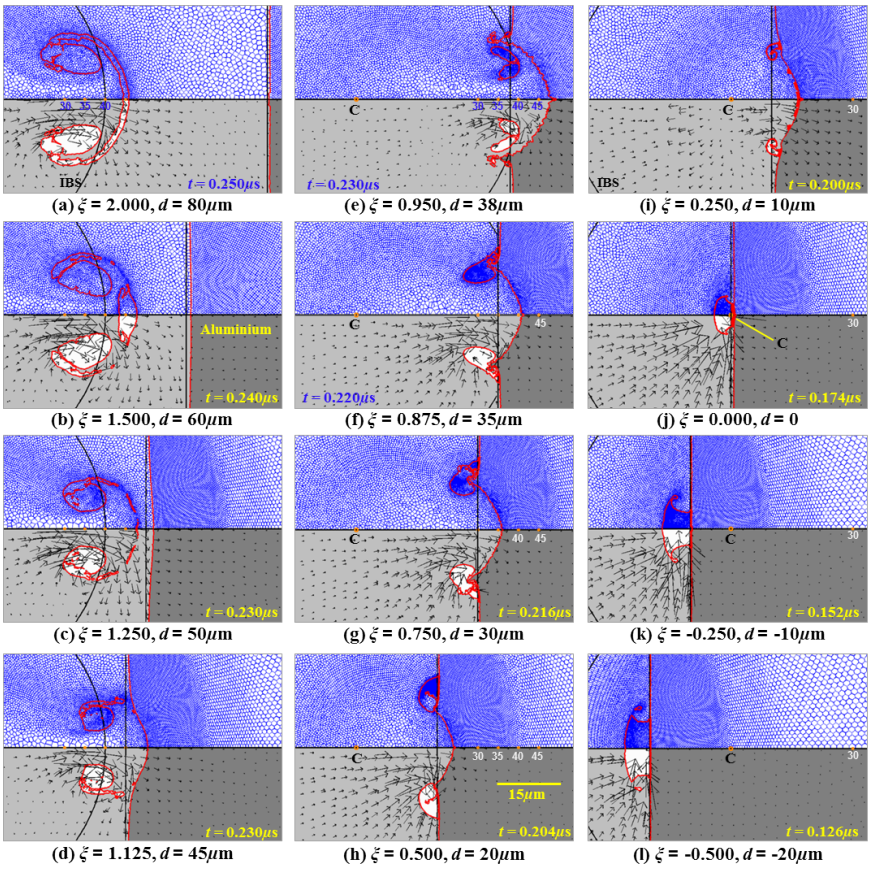

Figure 9. Plots of Voronoi mesh and velocity vectors showing how the mesh evolves with the flow for different ξ. These plots (given at different times) show the response of the aluminium as an elastic-plastic solid to the jetting collapse of the bubble, and the possible structural damage of the aluminium. The severe damage is associated with a direct or near direct impact of the axial jet from the collapsing bubbles residing very close to or attached to the aluminium, i.e. with $\xi = \{1.125, 0.95, 0.875, 0.75, 0.5, 0.25\}$.

the ideal gas EOS associated with this extreme pressure. Up to these times, therefore, no evidence of plastic deformation (crater) is observed except for a very minimal depression in the aluminium when $\xi = 0$ and -0.25. Lauer *et al.* [48] predicted the transformation from a mushroom to a 'pin'-shaped bubble (that later detaches from the wall) when the pinching continues by assuming the bubble to contain only vapour and the collapse is initiated by a higher uniform liquid pressure surrounding the bubble ('Rayleigh collapse'), i.e. two fundamental differences as compared to our scenarios of air-contained bubbles and the collapse is induced by a shock wave.

As shown in figure 10(a), for $\xi > 0$, the maximum jet velocity increases to reach the peak of about $2.31\,\mathrm{km/s}$ and gradually reduces to approach the $1.14\,\mathrm{km/s}$ mark of a free field bubble ($\xi = \infty$). For $\xi \leq 0$, although the bubble's upstream surface accelerates to the velocity of nearly $0.4\,\mathrm{km/s}$ or above, it does not transform into the axial high speed jet because of the nature of how these bubbles are attached to the wall and how they contract in response to the incident shock MS. The maximum depths of the crater can reach $> 13\,\mu\mathrm{m}$, i.e. for $\xi = \{0.95, 0.875, 0.75\}$ (figure 10(b)). For higher distances ξ, the depth reduces tremendously. The crater depth and size appears to correlate well with the speed of the axial jet and whether the impact is direct or indirect. Referring to figure 9, two types of crater are identified: (1) craters with a gradual and smooth edge,

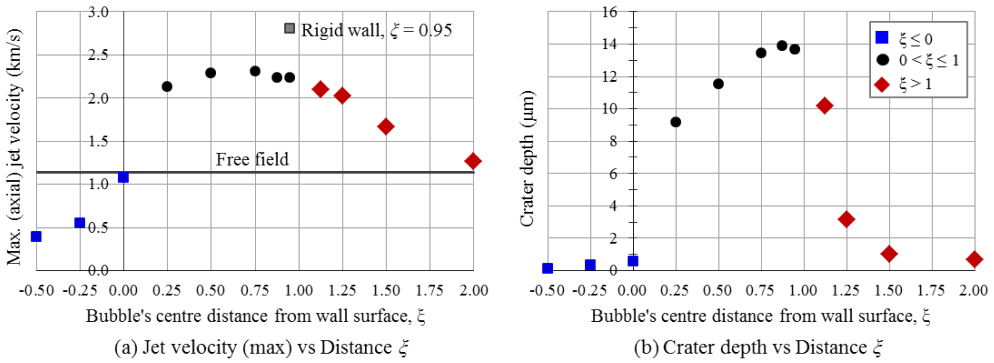

Figure 10. (a) The plot of maximum axial jet velocity (bubble's upstream surface) for different distances ξ. The cases for a bubble in free field (1.14 km/s) and attached to a rigid wall with $\xi = 0.95$ (2.8 km/s) are included for comparison. For $\xi = \{0, -0.25, -0.50\}$, the axial jet is not materialised. (b) The plot of crater depths for different distances ξ.

which are produced by either an indirect jet impact (e.g. with $\xi > 1$) or a direct jet impact coupled with an inward radial flow (e.g. with $\xi = 0.25$), and (b) craters with a sharp and well defined edge, which are produced almost solely by a direct jet impact (e.g. with $\xi = \{0.95, 0.875, 0.75, 0.5\}$).

(c) Comparison with experiment for a bubble attached to an aluminium foil

In the experiment by Philipp *et al.* [20], single bubbles ($150\,\mu$m-1.2 mm radius) were collapsed by a lithotripter shock. The shock peak pressure was about 65 MPa, and was generated using electrodes with a focusing ellipsoid (XL 1, Dornier Medizintechnik). The idealised pressure profile of the shock is shown in figure 11(b). The bubbles were attached to a $25\,\mu$m-thickness acrilate-coated polypropylene material that has an area density of $22.7\,\mathrm{g/m^2}$ and a tensile strength between 155 and $250\,\mathrm{N/mm^2}$. In our simulation, because of resource limitations only the case of $R_0 = 255\,\mu$m-radius bubble is simulated. As the acrilate-coated polypropylene material model is not available in the present scheme material database, aluminium is used instead to represent the elastic-plastic solid foil to which the bubble is attached to. The schematic of the computational domain is shown in figure 11(a). The equation for the idealised lithotripter shock pressure profile used in the experiment was not given, therefore, the shock profile used in the simulation was approximated using the equation (3.1), i.e. with values $P^+ = 40$ MPa, $\alpha_d = 7 \times 10^5\,\mathrm{s}^{-1}$, $f = 80$ kHz and $C_o = 5$. This shock reaches a pressure peak of $P_s \approx 65$ MPa. Initially, $46,918$ computational cells are used, i.e. 4920 for the air bubble, $39,461$ for water and 2537 for the foil.

The simulation presented in figure 12 shows the evolution of the Voronoi mesh that mimics the flow, the Schlieren-like (density gradient) that captures the shock propagation in the early stage of the interaction and the velocity vectors that indicate the flow direction at different times. The beginning of the interaction has similar features as the earlier simulations (including the expansion wave EW and transmitted shock TS). However, when the shock MS hits the aluminium foil, it is reflected as a shock and a rarefaction (seen as a two-wave structure in figure 12(b)) because the foil has a finite thickness. The contraction of the bubble causes a suction that sways the aluminium foil towards the centre of the bubble. The bubble's upstream surface eventually accelerates to form the high speed jet. At $t = 1.35\,\mu$s, the aluminium foil is seen to have moved to the $200\,\mu$m-mark on the symmetry axis. The high speed axial jet with velocity reaching 1.05 km/s impacts the foil at $t \approx 1.37\,\mu$s after the initiation. As shown in figure 12(i), at $t = 1.40\,\mu$s, the now-toroidal bubble shape is relatively thinner than that of the $40\,\mu$m-bubble attached to an aluminium wall. The impact of the jet pushes the foil downstream again, and the flow produces a vortex ring after the jet impact. The aluminium foil tends to stretch only without being penetrated by the jet at

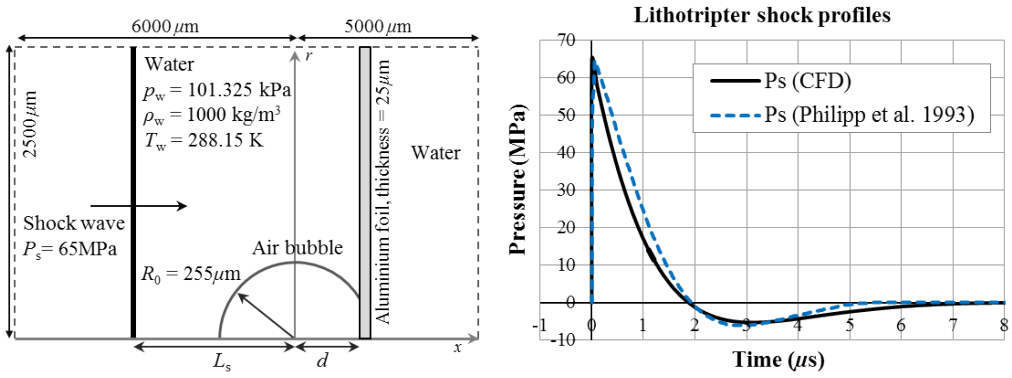

(a) Schematic of computational domain (b) Lithotripter shock profiles

Figure 11. (a) The schematic of the domain for the simulation of a lithotripter shock-induced collapse of a $255\,\mu$m-radius bubble attached to a $25\,\mu$m-thickness aluminium foil for a qualitative comparison with the experiment of Philipp *et al.* [20]. The aluminium foil model has $2785\,$kg/m^3 density, $26.5\,$GPa shear modulus and $0.3\,$GPa yield strength. $d = 242.25\,\mu$m and the bubble's centre distance is $\xi = d/R_0 = 0.95$. The shock is generated at a distance $L_s = 500\,\mu$m from the bubble's centre. (b) The lithotripter shockwave profiles used in the simulation and in the experiment.

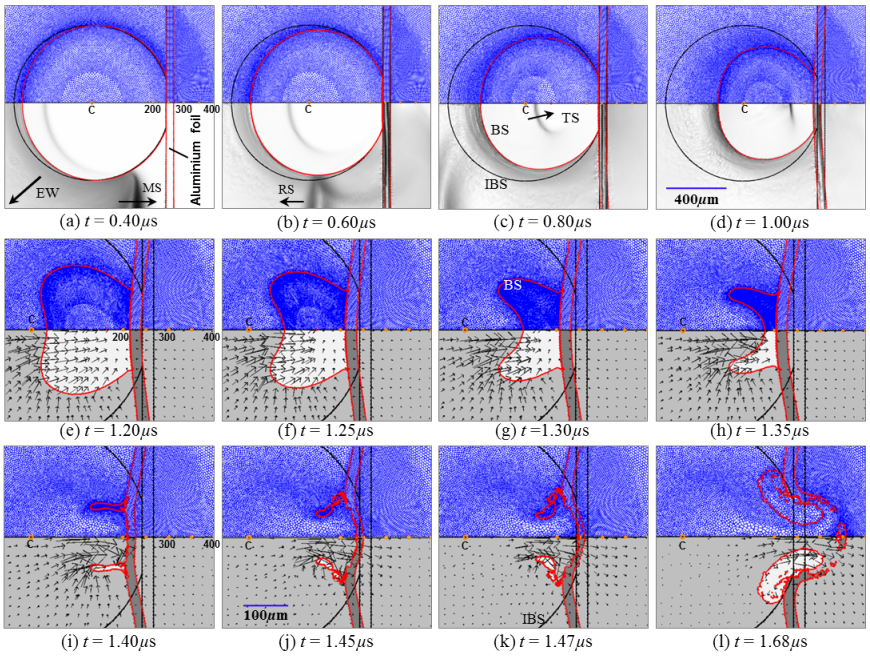

(a) $t = 0.40\mu$s (b) $t = 0.60\mu$s (c) $t = 0.80\mu$s (d) $t = 1.00\mu$s
(e) $t = 1.20\mu$s (f) $t = 1.25\mu$s (g) $t = 1.30\mu$s (h) $t = 1.35\mu$s
(i) $t = 1.40\mu$s (j) $t = 1.45\mu$s (k) $t = 1.47\mu$s (l) $t = 1.68\mu$s

Figure 12. The plots of Voronoi mesh (top half) with Schlieren-like (bottom half) and Voronoi mesh with velocity vectors (bottom half) that show the interaction of the lithotripter shock wave with a single bubble attached to an aluminium foil. The foil tends to sway together with the flow but is eventually pierced by the high speed jet from the collapsing bubble.

least until $t = 1.47\,\mu$s. However, the foil is eventually pierced, which appears to be caused by both the flow behind the jet and the expansion of the toroidal bubble (figure 12(l)). Some aluminium fragments are carried downstream by the flow.

The maximum jet velocity of $1.05\,\mathrm{km/s}$ is substantially lower than the $2.16\,\mathrm{km/s}$ of that with $40\,\mu$m-radius bubble. This may be due to factors such as the relative size of the bubble with respect to the lithotripter shock peak pressures and the type of boundary being used, i.e. aluminium foil instead of aluminium wall. When compared to the experiment by Philipp *et al.* [20], both the experiment and simulation show that the foil are pierced by the collapse of the bubble. Although the size of the hole is similar, i.e. $\approx 150\,\mu$m, the patterns are quite different. In the experiment, it looks as though the foil was torn, which may be typical of materials made of plastics. In the simulation, the aluminium foil is seen to be fragmented by the flow. For decades, the pitting of aluminium foil has been the preferred method by which industry has found a proxy for the cleaning performance of an ultrasonic cleaning bath [54]. Whilst 'cavitation jets' have been the accepted explanation for the formation of punctures in the foil, this is the first simulation of the process, which allows prediction of the magnitudes of the forces at play, the material responses, and the details of the mechanism.

4. Conclusion

The free-Lagrange scheme, FLM, that incorporates the compressibility, multi-phases and elastic-plastic solid models has been used to simulate the collapse of $40\,\mu$m-radius single bubbles attached to/near rigid and aluminium walls by a $60\,$MPa-lithotripter shock, and the collapse of a $255\,\mu$m-radius bubble attached to a $25\,\mu$m-thick aluminium foil by a $65\,$MPa-lithotripter shock. The collapse events of the bubble attached to the aluminium is different from that with a rigid wall because the aluminium is allowed to deform after the jet and the blast wave impingement. The study of the collapse for different distances ξ from the aluminium ($\xi > 1$, $0 < \xi \leq 1$ and $\xi \leq 0$) shows different characteristics in the collapse dynamics (i.e. bubble jetting or bubble pinching) and different damage/crater patterns (i.e. gradual and smooth edge or sharp and well defined edge with material ejection). The results strongly indicate that the deformation in solids subjected to cavitation and shock interaction is primarily associated with the direct or near direct impact of the axial jet from collapsing bubbles attached or residing very close to the solids (i.e. $0 < \xi < 1.25$), and the blast wave impact appears to be only the secondary cause. The damage patterns, e.g. for $\xi = \{0.95, 0.875, 0.75, 0.5\}$, exhibit characteristics similar to those of the high speed projectile impact. The qualitative comparison with the experiment for the $255\,\mu$m-radius bubble attached to $25\,\mu$m-thickness foil shows that the bubble jetting collapse pierces the foil with a similar sized hole but with a different hole patterns owing to different material properties of the foils. With the use of the elastic-perfectly plastic material model, we are able to model the response of the solid under extreme loading in the context of shock-induced bubble collapse. An improvement in the constitutive models, e.g. with the use of Johnson & Cook model [55], may further enhance the applicability of the current scheme to model the yield of solid materials more accurately.

Data accessibility. This work does not have any experimental data.
Competing interests. We have no competing interests.
Authors' contributions. All authors had equal contribution and gave approval for publication.

Acknowledgements. A.R. Jamaluddin. was supported through a PhD studentship provided by the EPSRC (grant no. GR/N19243; Principal Investigator: T.G. Leighton).
The data supporting this study are openly available as DOI: TO-BE-INSERTED-IF-ACCEPTED from the University of Southampton repository at http://dx.doi.org/TO-BE-INSERTED-IF-ACCEPTED.

References

1. Ball GJ, Howell BP, Leighton TG, Schofield MJ. 2000 Shock-induced collapse of a cylindrical air cavity in water: a Free-Lagrange simulation. *Shock Waves* **10**, 265–276.
2. Bourne NK, Field JE. 1999 Shock-induced collapse and luminescence by cavities. *Proc. Roy. Soc. Lond. A* **357**, 295–311.

3. Hawker NA, Ventikos Y. 2012 Interaction of a strong shockwave with a gas bubble in a liquid medium: a numerical study. *J. Fluid Mech.* **132**, 1–39.
4. Jamaluddin AR, Ball GJ, Turangan CK, Leighton TG. 2011 The collapse of single bubbles an approximation of the far field acoustic emissions for cavitation induced by shock wave lithotripsy. *J. Fluid Mech.* **677**, 305–341.
5. Turangan CK, Jamaluddin AR, Ball GJ, Leighton TG. 2008 Free-Lagrange simulations of the expansion and jetting collapse of air bubbles in water. *J. Fluid Mech.* **598**, 1–25.
6. Zhang S, Duncan J, Chahine GL. 1993 The final stage of the collapse of a cavitation bubble near a rigid wall. *J. Fluid Mech.* **257**, 147–1993.
7. Brennen CE. 1995. *Cavitation and Bubble Dynamics*. Oxford University Press.
8. Klaseboer E, Hung KC, Wang C, Wang CW, Khoo BC, Boyce P, Debono S. 2005 Experimental and numerical investigation of the dynamics of an underwater explosion bubble near a resilient/rigid structure. *J. Fluid Mech.* **537**, 378–413.
9. Leighton TG, Cleveland RO. 2010 Lithotripsy. *Proc. Inst. Mech. Engineers, Part H: J. Engineering in Med.* **224**(2), 317–342. (doi: 10.1243/09544119JEIM588)
10. Bourne NK, Field JE. 1991 Bubble collapse and the initiation of explosion. *Proc. Roy Soc. Lond. A* **435**, 423–435.
11. Bourne NK, Milne JE. 2003 The temperature of shock-collapsed cavity. *Proc. Roy. Soc. Lond. A* **459**, 1851–1861.
12. Ohl CD, Ikink R. 2003 Shock-wave-induced jetting of micron-size bubbles. *Phys. Rev. Lett.* **21**, 214502.
13. Tandiono, Ow DSW, Driessen L, Chin CSH, Klaseboer E, Choo ABH, Ohl SW, Ohl CD. 2012 Sonolysis of Escherichia coli and Pichia pastoris in microfluidics. *Lab on a Chip* **12**(4), 780–786.
14. Birkin PR, Offin DG, Vian CJB, Howlin RP, Dawson JI, Secker TJ, Herve RC, Stoodley P, Oreffo ROC, Keevil CW, Leighton TG. 2015 Cold water cleaning of brain proteins, biofilm and bone - harnessing an ultrasonically activated stream. *Phys. Chemistry Chem. Phys.* **17**, 20574–20579.
15. Howlin RP, Fabbri S, Offin DG, *et al*. 2015 Removal of dental biofilms with a novel ultrasonically-activated water stream. *J. Dental Res.* **94**(9), 1303–1309, (Electronic supplementary material: http://eprints.soton.ac.uk/377535/).
16. Leighton TG. 2017 The acoustic bubble: Ocean, cetacean and extraterrestrial acoustics, and cold water cleaning. *IOP J. of Phys.: Conference Series* **797**, 012001.
17. Field JE. 1991 The physics of liquid impact, shock wave interactions with cavities, and the implications to shock-wave lithotripsy. *Phys. Med. Biol.* **36**(11), 1475–1484.
18. Anderson P, Hawker N, Betney M, Tully B, Ventikos Y, Roy RA. 2013 Experimental characterisation of light emission during shock-driven cavity collapse. *Proc. on Meetings in Acoustics 19*. The Acoust. Soc. of Am. - American Institute of Physics.
19. Kodama T, Takayama K. 1998 Dynamic behaviour of bubbles during extracorporeal shock-wave lithotripsy. *Ultrasound in Med. Biol.* **24(5)**, 723–738.
20. Philipp A, Delius M, Scheffczyk C, Vogel A, Lauterborn W. 1993 Interaction of lithotripter-generated shock waves with air bubbles. *J. Acoust. Soc. Am.* **93(5)**, 2496–2509.
21. Leighton TG, Turangan CK, Jamaluddin AR, Ball GJ, White PR. 2013 Prediction of far-field acoustic emissions from cavitation clouds during shock wave lithotripsy for development of a clinical device. *Proc. Roy. Soc. A* **469**, 21pp. (doi: 10.1098/rspa.2012.0538)
22. Leighton TG, Fedele F, Coleman AJ, McCarthy C, Ryves S, Hurrell AM, Stefano AD, White PR. 2008 A passive acoustic device for real-time monitoring the efficacy of shockwave lithotripsy treatment. *Ultrasound Med. Biol.* **34**(10), 1651–1665.
23. Ding Z, Gracewski SM. 1996 The behaviour of a gas cavity impacted by a weak or strong shock wave. *J. Fluid Mech.* **309**, 183–209.
24. Nourgaliev RR, Dinh TN, Theofanous TG. 2006 Adaptive characteristics-based matching for compressible multi-fluid dynamics. *J. Comput. Phys.* **213**(2), 500–529.
25. Johnsen E, Colonius T. 2009 Numerical simulations of non-spherical bubble collapse. *J. Fluid Mech.* **629**, 231–262.
26. Kobayashi K, Kodama T, Takahira H. 2011 Shock wave-bubble interaction near soft and rigid boundaries during lithotripsy: numerical analysis by the improved ghost fluid method. *Phys. in Med. and Biol.* **56**(19), 6421–6440.
27. Klaseboer E, Turangan CK, Fong SW, Liu TG, Hung KC, Khoo BC. 2006 Simulations of pressure-pulse bubble interaction using boundary element method. *Comput. Methods Appl. Engng.* **195**, 4287–4302.

28. Klaseboer E, Fong SW, Turangan CK, Khoo BC, Szeri AJ, Calvisi ML, Sankin GN, Zhong P. 2007 Interaction of lithotripter shockwaves with single inertial cavitation bubbles. *J. Fluid Mech.* **593**, 33–56.
29. Wang Q. 2015 Bubble dynamics in a compressible liquid in contact with a rigid boundary. *Interface Focus* **5(5)**. (doi:10.1098/rsfs.2015.0048)
30. Blake JR, Taib BB, Doherty G. 1986 Transient cavities near boundaries. Part 1: Rigid boundary. *J. Fluid Mech.* **170**, 479–497.
31. Freund JB, Shukla RK, Evan AP. 2009 Shock-induced bubble jetting into a viscous fluid with application to tissue injury in shock-wave lithotripsy. *J. Acoust. Soc. Am.* **126**(5), 2746–2756.
32. Xie WF, Young YL. 2007 Two-dimensional shock induced collapse of gas bubble near a semifinite deformable solid. *J. Mech. Materials and Structures* **2**(10), 1881–1900.
33. Chahine GL. 2014 Modeling of cavitation dynamics and interaction with material, Ch. 6 in Kim KH *et al.*: Advanced experimental and numerical techniques for cavitation erosion prediction. *Fluid Dyn. and its Applications* **160**, 123–173.
34. Chahine GL, Hsiao C-T. 2015 Modeling cavitation erosion using fluid-material interaction simulations. *Interface Focus* **5**, 20150016.
35. Hsiao C-T, Jayaprakash A, Kapahi A, Choi J-K, Chahine GL. 2014 Modeling of material pitting from cavitation bubble collapse. *J. Fluid Mech.* **755**, 142–175.
36. Howell BP, Ball GJ. 2000 Damping of mesh-induced errors in free-Lagrange simulations of Richtmyer-Meshkov instability. *Shock Waves* **10**, 253–264.
37. Howell BP, Ball GJ. 2002 A free-Lagrange augmented Godunov method for the simulation of elastic-plastic solids. *J. Comput. Phys.* **175**, 128–167.
38. Turangan CK. 2004 *Free-Lagrange simulations of cavitation bubble collapse*. PhD Thesis, University of Southampton, UK.
39. Baik K, Jiang J, Leighton TG. 2010 Acoustic attenuation, phase and group velocities in liquid-filled pipes: Theory, experiment, and examples of water and mercury. *J. Acoust. Soc. Am.* **128**(5), 2610–2624. (doi: 10.1121/1.3495943)
40. Jiang J, Baik K, Leighton TG. 2011 Acoustic attenuation, phase and group velocities in liquid-filled pipes II: Simulation for spallation neutron sources and planetary exploration. *J. Acoust. Soc. Am.* **130**(2), 695–706. (doi:10.1121/1.3598463)
41. Leighton TG, Baik K, Jiang J. 2012 The use of acoustic inversion to estimate the bubble size distribution in pipelines. *Proc. Royal Soc. A* **468**, 2461–2484. (doi:10.1098/rspa.2012.0053)
42. Ball GJ. 1996 A Free-Lagrange method for unsteady compressible flow: simulation of a confined cylindrical blast wave. *Shock Waves* **5**, 311–325.
43. Harten A, Lax PD, van Leer B. 1983 On upstream differencing and Godunov-type scheme for hyperbolic conservation law. *SIAM Review* **25**(1), 35–61.
44. Flores J, Holt M. 1981 Glimm's method applied to underwater explosions. *J. Comput. Phys.* **44**, 377–387.
45. Dukowicz JK. 1985 A general, non-iterative Riemann solver for Godunov's method. *J. Comput. Phys.* **61**, 119–137.
46. Wilkins ML. 1999 *Computer simulation of dynamic phenomena*, Springer.
47. Cunningham KB, Coleman A, Leighton TG, White PR. 2001 Characterising *in vivo* acoustic cavitation during lithotripsy with time-frequency methods. *Acoustics Bulletin* **26**(5), 10–16.
48. Lauer E, Hu XY, Hickel S, Adams NA. 2012 Numerical modelling and investigation of symmetric and asymmetric cavitation bubble dynamics. *Computers & Fluids* **69**, 1–19.
49. Church CC. 1989 A theoretial study of cavitation generated by an extracorporeal shock wave lithotripter. *J. Acoust. Soc. Am.* **86**, 215–227.
50. Leighton TG. 2007 What is ultrasound? *Prog. Biophysics & Molecular Biol.* **93**(1-3), 3–83.
51. Haller KK, Poulikakos D, Ventikos Y, Monkewits P. 2003 Shock wave formation in droplet impact on a rigid surface: lateral liquid motion and multiple wave structure in the contact line region. *J. Fluid Mech.* **490**, 1–14.
52. Brunton JH. 1967 *Proc. Int. Conf. Rain Eros., 2^{nd} ed.* pp.291, Royal Aircraft Establishment, Farnborough, United Kingdom.
53. Leighton TG. 1994 *The acoustic bubble*, The Academic Press, London.
54. Leighton TG, Birkin PR, Hodnett M, *et al*. 2005 Characterisation of measures of reference acoustic cavitation: An experimental feasibility trial. *In AA Doinikov, ed. Bubble & Particle Dynamics in Acoustic Fields: Modern Trends & Applications, Research Signpost, Kerala*, 37–94.
55. Johnson GR, Cook WH. 1983 A constitutive model and data for metals subjected to large strains, high strain rates and high temperatures. *The 7^{th} Int. Symp. on Ballistics*, 541–547.